

Use of compliant actuators for throwing rigid projectiles

Guillaume Giombini ¹, Joachim Mathiesen,² Christophe D'Angelo ¹, Médéric Argentina,¹ Christophe Raufaste ^{1,3} and Franck Celestini ¹

¹Université Côte d'Azur, CNRS, Institut de Physique de Nice (INPHYNI), 06100 Nice, France

²Niels Bohr Institute, University of Copenhagen, Copenhagen, Denmark

³Institut Universitaire de France (IUF), 75005 Paris, France



(Received 25 February 2021; revised 1 December 2021; accepted 10 December 2021; published 1 February 2022)

Muscles and tendons, actuators in robotics, and various sports implements are examples that exploit elasticity to accelerate objects. Tuning the mechanical properties of elastic elements connecting objects can greatly enhance the transfer of mechanical energy between the objects. Here, we study experimentally the throw of rigid projectiles by an actuator, which has a soft elastic element added to the distal end. We vary the thickness of the elastic layer and suggest a simple mass-spring chain model to find the properties of the elastic layer, which will maximize the energy transfer from the actuator to the projectile. The insertion of a soft layer, impedance matched to the ejection frequency of the projectile mass, can increase the throwing efficiency by over 400%. Finally, we identify that very thick and very soft compliant layers could potentially lead to high efficiency and flexibility simultaneously.

DOI: [10.1103/PhysRevE.105.025001](https://doi.org/10.1103/PhysRevE.105.025001)

I. INTRODUCTION

The elasticity of tendons can be exploited to increase muscle-powered acceleration [1–5], for example, when jumping [6–9], running [10,11], or throwing [12,13]. In order to better understand the interaction between muscles and tendons or to develop compliant actuators in robotics, models of connected elastic elements have been suggested, e.g., in Refs. [14–20]. In sports, the acceleration of balls is initiated by a kick, hit, or a throw [21]. The hit of a ball usually relies on sport implements (racket, club, bat, etc). Phomsoupha *et al.* [22] have shown that the elasticity of the badminton racket can increase the velocity of its head by a factor 1.8 as compared to a rigid one. The same could hold for other slender implements that can bend, for example a golf shaft, which undergoes a significant deformation [23] that increases the club head velocity [24,25].

The throw of a projectile can similarly benefit from introducing a compliant contact layer. For example, soft elastic projectiles or rigid projectiles with soft elastic contact layers [26,27] can improve the transfer of energy by a factor of 250–300%. In these studies, it is shown that a precise synchronization is required to achieve an optimal energy transfer. For example, the time scale of the actuator has to match the time scale of the wave propagation in the projectile [26,27].

In this article, we investigate the role of adding a soft elastic layer at the distal end of an actuator used to throw rigid projectiles. Whereas our system might resemble the system considered in Celestini *et al.* [27], it exhibits a difference in boundary conditions that modifies the dynamics driven by the propagation of elastic waves inside the soft layer. As we shall see below, the fact that this layer is attached to the actuator instead of to the projectile gives rise to a complex efficiency landscape and ultimately permits an energy transfer factor above 400%. Our study combines experiments, numerical simulations, and theory.

We employ a compliant actuator composed of a plate on which is glued an elastic soft layer of thickness L_s [Figs. 1(a) and 1(b)]. The plate accelerates from rest at time $t = 0$ and undergoes a harmonic variation given by

$$z_p(t) = A[1 - \cos(2\pi ft)], \quad (1)$$

with a frequency f and an amplitude A . The maximum velocity of the plate is $V_p^* = 2\pi fA$. A rigid projectile, of mass m , which is located at $z = z_m(t)$, is accelerated by the actuator, and is ejected at time t_e with a velocity $V_e = \dot{z}_m(t_e)$. The efficiency of the throw is quantified by the energy transfer factor $\alpha = (V_e/V_p^*)^2$. This coefficient characterizes the gain or loss of kinetic energy as compared to the ejection of a rigid projectile that is expected to take off from the substrate with $V_e = V_p^*$ or $\alpha = 1$ [26,27]. To provide some insights, we can consider the elastic soft layer as an ideal massless linear spring with a stiffness k . If we note $f_0 = \frac{1}{2\pi} \sqrt{\frac{k}{m}}$ the eigenfrequency of the spring-mass system, α reaches a maximum 3.13 for $f_0/f \simeq 1.62$, which emphasizes the role of synchronization to enhance energy transfers (see Celestini *et al.* [27] or Appendix A).

In what follows we consider the soft layer of section S as a continuous medium with density ρ_s and elastic modulus E_s . Such material does not deform uniformly as an ideal spring and elastic waves traveling in the soft layer need to be considered. As we will see, such systems permit an energy transfer factor above 4.

II. MATERIAL AND METHODS

A. Experiments

The experiments are performed with an ejection engine, whose uniaxial motion can be described by the dynamics of a damped harmonic oscillator (Fig. 2). The frequency

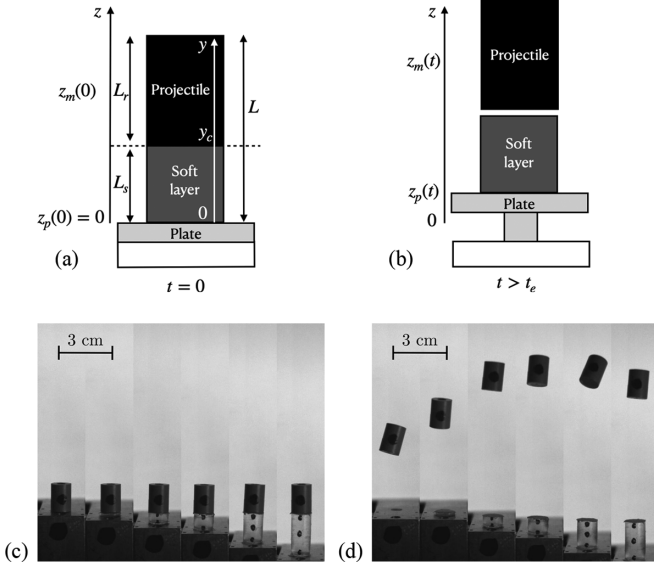


FIG. 1. (a),(b) Compliant actuator: a plate is accelerating from rest at $t = 0$, on which is glued an elastic soft layer. A rigid projectile is deposited on the top of this actuator (a) at time $t = 0$ and (b) just after the ejection $t > t_e$. (c),(d) Ejection at $f = 63.2$ Hz of 16.3 mm long rigid projectiles and different lengths of soft layer, from left to right: 0, 2.0, 5.6, 9.5, 16.8, and 23.4 mm. Dark circular spots are used to track the position of each component over time. The whole image sequences are shifted vertically so that ejection occurs at the same height in all cases. Images are taken at the time of ejection t_e (a) and 56.8 ms after ejection (b). Movies are available in the Supplemental Material [28].

f is measured by interpolating the time evolution of the plate position with the equation of an underdamped oscillator (Appendix D). In all experiments, the damping ratio is small, around 6.4×10^{-2} , so that the expression of $z_p(t)$ given in Eq. (1) remains a good approximation to describe the plate motion from $t = 0$ to the ejection time t_e . The frequency f of the engine can be varied in the interval 20–80 Hz (here we use two values, 31.1 and 63.2 Hz) and the amplitude A is approximately 2 mm. The maximum velocity of the engine, $V_p^* \simeq 2\pi f A$, is around 0.8 m s^{-1} and the typical acceleration is around 3–16 g with g the standard gravity. Moreover, the weights m of the projectiles are negligible relative to the weight of the engine and therefore do not influence the engine motion.

We use cylindrical projectiles with a diameter of 12 mm and a length L_r of (8.2 ± 0.1) mm or (16.3 ± 0.1) mm. They are made of a rigid material, polyether ether ketone, with Young modulus $E_r = 3.6 \text{ GPa}$, density $\rho_r = 1300 \text{ kg m}^{-3}$, and wave velocity $c_r = \sqrt{E_r/\rho_r} = 1700 \text{ m s}^{-1}$. These projectiles are not directly in contact with the throwing engine but a soft elastic layer (same diameter 12 mm) is introduced between the engine and the projectile. This layer is composed of a hydrogel made from powdered gelatin (Sigma-Aldrich, gelatin from porcine skin, gel strength 300, type A) dissolved in water for 30 min at 80°C under gentle agitation with a powder to water mass concentration around 15%. The aqueous solution is then poured into cylindrical molds and kept at rest for a few hours, until the layers are reticulated. The density of

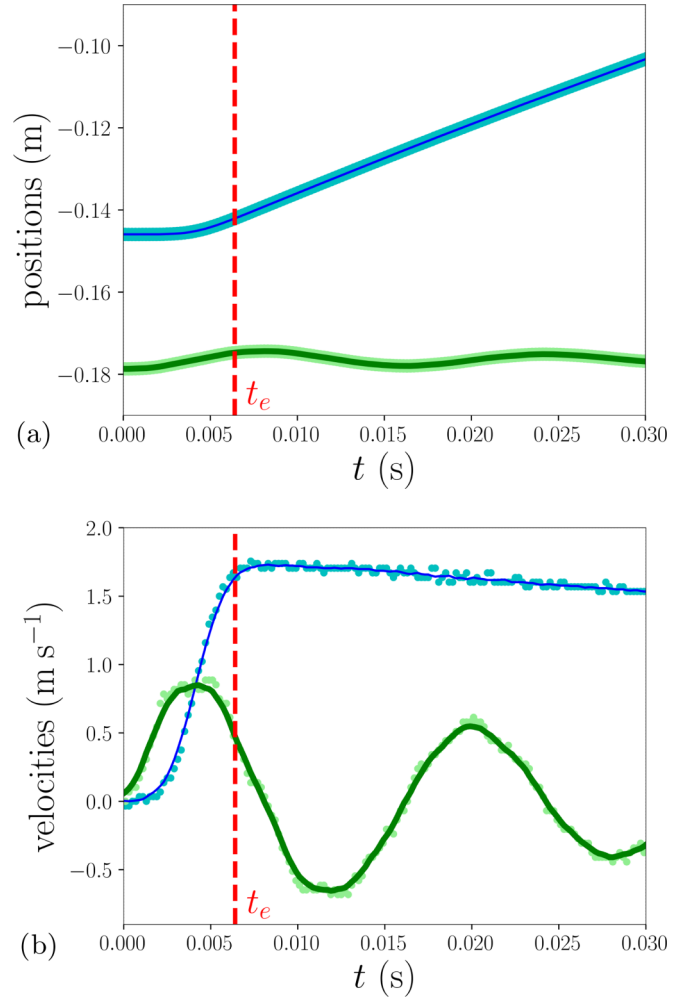


FIG. 2. (a) Position of the projectile (thin blue line) and of the engine plate (thick green line) as functions of time for the following parameters: $L_r = 8.2$ mm, $L_s = 16.8$ mm, and $f = 63.2$ Hz. (b) Velocities obtained by centered difference of the positions after running averages.

the layer is $\rho_s = 1000 \text{ kg m}^{-3}$. Several lengths L_s were used among 2.0, 5.6, 9.5, 16.8, 23.4, and 29.1 mm with a precision of 0.1 mm. The wave velocity is inferred by characterizing the deformation dynamics of the soft layer alone, see Appendix B, and we measure $c_s = 7.8 \pm 0.3 \text{ m s}^{-1}$ (the Young modulus is thus around $E_s = c_s^2 \rho_s \simeq 61 \text{ kPa}$) after statistics over all lengths. Characteristics of the hydrogels are measured before and after experiments and we have checked that they do not vary significantly: the lengths of the soft layers vary by less than 5% in experiments and the same stands for the wave velocity. Adhesion between the soft layer and the engine plate is ensured with a thin film of vacuum grease. A thin piece of blotting paper is introduced between the soft layer and the rigid projectile: it adheres to the soft layer and keeps the rigid projectile free to detach. As observed in the movies (see the Supplemental Material [28]), the deformation is smaller than 10% and the soft layer is mostly deformed in the linear elastic regime [29].

We define $x = L_s/L$ as the ratio between the length of the soft layer and the total length $L = L_r + L_s$ of the soft

and rigid parts. Three sets of experiments were performed. For each set, the frequency f and the length L_r of the rigid projectile are fixed, and the length L_s of the soft layer is varied systematically. One set of experiments is displayed in Fig. 1 with $f = 63.2$ Hz and $L_r = 16.3$ mm. Varying L_s tunes the two dimensionless quantities c_s/Lf and x . The two other sets of experiments were performed with [$f = 63.2$ Hz and $L_r = 8.2$ mm] and [$f = 31.1$ Hz and $L_r = 8.2$ mm], respectively.

The dynamics of the experiments are recorded with a high-speed camera (5000 frames per s) and each experiment is repeated three times for statistics. The positions $z_m(t)$ of the rigid part and $z_p(t)$ of the engine plate are tracked over time from the recorded videos thanks to a Python tracking script [Fig. 2(a)]. The respective velocities $V_m(t)$ and $V_p(t)$ are obtained by differentiating the positions [Fig. 2(b)]. We note V_e the ejection velocity of the rigid projectile at the ejection time t_e . Both V_e and V_p^* are inferred by measuring the maximal velocities of $V_m(t)$ and $V_p(t)$, respectively.

B. Numerical simulations

In addition to the experiments, we have performed numerical simulations of projectile ejection using a basic linear-elastic model. Since $c_r \gg c_s$, we can consider the projectile as infinitely rigid and expect its mass $m = \rho_r SL_r$ to be the only relevant feature of the projectile. In our numerical approach described in Celestini *et al.* [27], we consider the projectile as a one-dimensional (1D) material with waves traveling inside both the rigid projectile and the soft layer, and vary L_r instead of m without loss of generality.

The deformation dynamics is described by the one-dimensional momentum balance or wave equation for the displacement field $u(y, t)$ [27],

$$\rho(y)\partial_t^2 u(y, t) - \partial_y[E(y)\partial_y u(y, t)] = 0. \quad (2)$$

Here $y \in [0, L]$ is the distance in the undeformed frame to the ejection engine bottom plate, $E(y)$ is the local Young modulus, and $\rho(y)$ is the mass density.

The deformation in both the soft layer and in the rigid projectile is described by the same equation and we note u_s ($y \in [0, y_c]$) and u_r ($y \in [y_c, L]$) the displacement in the soft and rigid parts, respectively, with $y_c = L_s$ the contact point between the projectile and soft layer [Fig. 1(a)]. The material parameters are assumed to be constant throughout the soft contact layer and in the projectile. In both the soft layer and the projectile, the deformation is described by the wave equation with two longitudinal wave velocities, $c_s = \sqrt{E_s/\rho_s}$ and $c_r = \sqrt{E_r/\rho_r}$. For the numerical simulations we used a basic semi-implicit (symplectic) Euler finite difference scheme. The bottom end of the contact layer follows the speed of the actuator plate. The dynamics is therefore subject to the following boundary conditions assuming a harmonic motion of the plate (up to the point when the projectile is ejected):

$$\text{BCs} \begin{cases} u_s(0, t) & = A[1 - \cos(2\pi ft)], \\ E_s \partial_y u_s(y_c, t) & = E_r \partial_y u_r(y_c, t), \quad \text{for } t < t_e, \\ \partial_t u_s(y, 0) & = 0, \quad \text{for } y < y_c, \\ \partial_t u_r(y, 0) & = 0, \quad \text{for } y > y_c, \\ \partial_y u_r(y, t) & \xrightarrow{y \rightarrow L} 0. \end{cases} \quad (3)$$

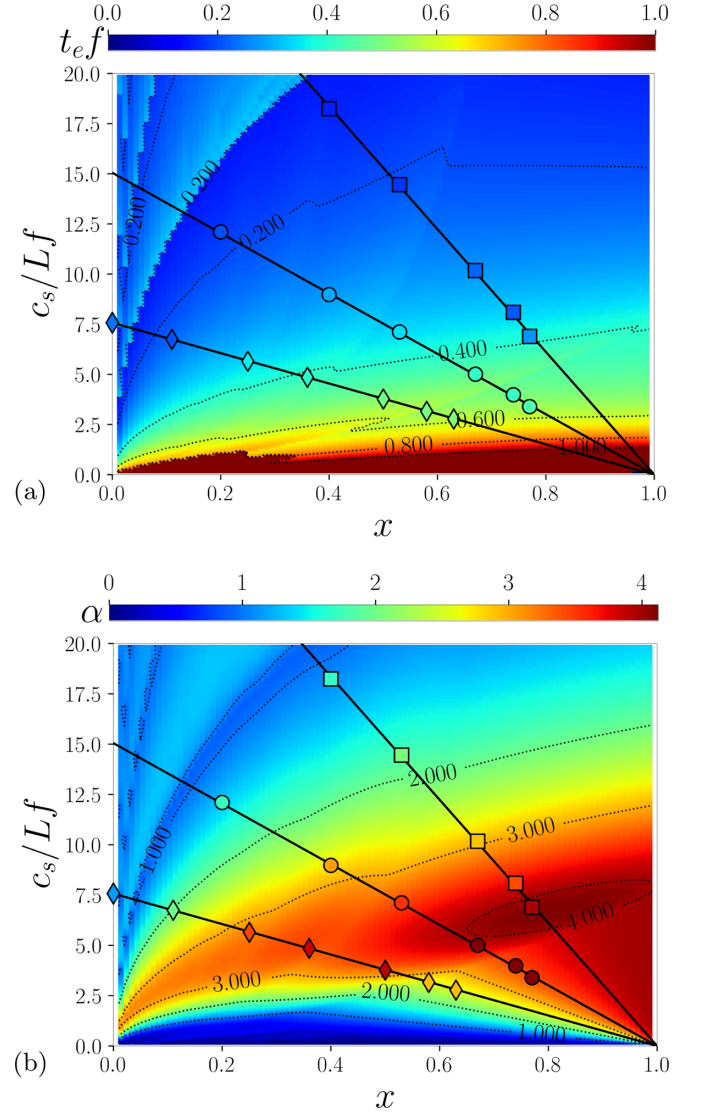


FIG. 3. Comparison between experiments and simulations: $t_e f$ (a) and α (b) as functions of x and c_s/Lf . The three sets of experiments correspond to $c_s/L_r f = 7.57$ (diamonds), 15.1 (disks), and 34.5 (squares).

In our simulations, the projectile is released from the throwing engine as soon as the strain crosses from positive to negative value at $y = y_c$. At this point, the displacement loses continuity and the projectile is released. This means that the condition $E_s \partial_y u_s(y, t) = E_r \partial_y u_r(y, t)$ is replaced by $0 = \partial_y u_s(y, t) = \partial_y u_r(y, t)$. Note that it is possible for a projectile to reconnect to the engine after a first takeoff. Consequently, we might observe in simulations successive stages of ejection and reconnection. Simulations have been performed for the case of an underdamped harmonic oscillator as well (Appendix D) with the damping factor found experimentally. Since the two approaches showed little differences, we present the harmonic case only in what follows.

III. RESULTS

In Fig. 3, both the dimensionless ejection time $t_e f$ and the energy transfer factor α are represented with a 2D color plot

as functions of x and c_s/Lf on the axes. Both numerical and experimental data are represented. From the simulations, we find that the dimensionless ejection time $t_e f$ ranges between 0.25 (the value expected without soft layer) on the c_s/Lf axis to ∞ on the x axis [Fig. 3(a)]. The region with $t_e f > 1$ is restricted to a narrow band close to the x axis. This region is characterized by several cycles of the throwing engine and by an inefficient transfer of energy as attested by the α plot in Fig. 3(b).

The experimental data are superimposed in Fig. 3 as symbols with colors from the same color scale used for the simulations in the background. Three sets of experiments have been performed and each of them corresponds to a given rigid length L_r and a given plate frequency f , while the length of the soft layer is varied. As a consequence, one set of experiments is aligned in the 2D space along the linear functions of equation $c_s/Lf = (1-x)c_s/L_r f$, with $c_s/L_r f$ constant for a given set of experiments. In Fig. 3, three sets of experiments are displayed with $c_s/L_r f = 7.57$ (diamonds), 15.1 (disks), and 34.5 (squares). The results seem in good agreement with the values obtained in the simulation, both for $t_e f$ and α . In general, the energy transfer factor exhibits a complex behavior in our 2D parameter space. α equals 0 on both axes and has two regions with large values. One of them is centered around $x = 0.8$ and $c_s/Lf = 6.7$ with a maximum value $\alpha = 4.12$. The second is a line segment where $\alpha = 4$ for $x = 1$ and c_s/Lf between 0 and 7.9. In Fig. 4 we represent the coordinates and values of the maximal α value found in simulation along a vertical line in the α diagram as functions of x . The limit $x \rightarrow 0$ is very similar to a previously studied case where the soft layer is attached to the projectile instead of to the actuator [27]: the optimal values are found along a curve described by the expression $c_s/Lf = 10.2\sqrt{x}$ and achieves a maximum $\alpha = 3.13$. The nature of the contact does not seem to play a role for small values of x around this curve. It corresponds to a quasistatic limit where the deformation of the soft layer is homogeneous and the time $t_s = L_s/c_s$ for the wave to travel inside the soft layer is much shorter than the ejection time $t_e \gg t_s$. Our system where the soft layer is attached to the actuator exhibits maximal α values that are significantly larger than 3.13. We will see in Sec. IV that this corresponds to a dynamical regime where $t_e \gtrsim t_s$. It explains the discontinuities and changes of trend observed in Fig. 4 as well.

In Fig. 5, we compare directly experiments and simulations along the lines passing through the experimental data. We observe that experiments and simulations follow the same trends for the three sets of data and the energy transfer factor can be as high as 4 in both cases if parameters are well chosen. Deviations are observed between the two approaches in some cases, which is not surprising given that the experimental system is not perfect nor 1D, as biological systems are [20]. Apart from the geometry, several other effects omitted in the model could play a role in this system. This includes the exact kinematics of the plate motion, a more advanced description of the contacts between the plate and the soft layer and between the soft layer and the rigid projectile, respectively, or the need to account for the precise rheological properties of the gelatin layer for instance. We have kept the model as simple as possible and without free parameters to catch the

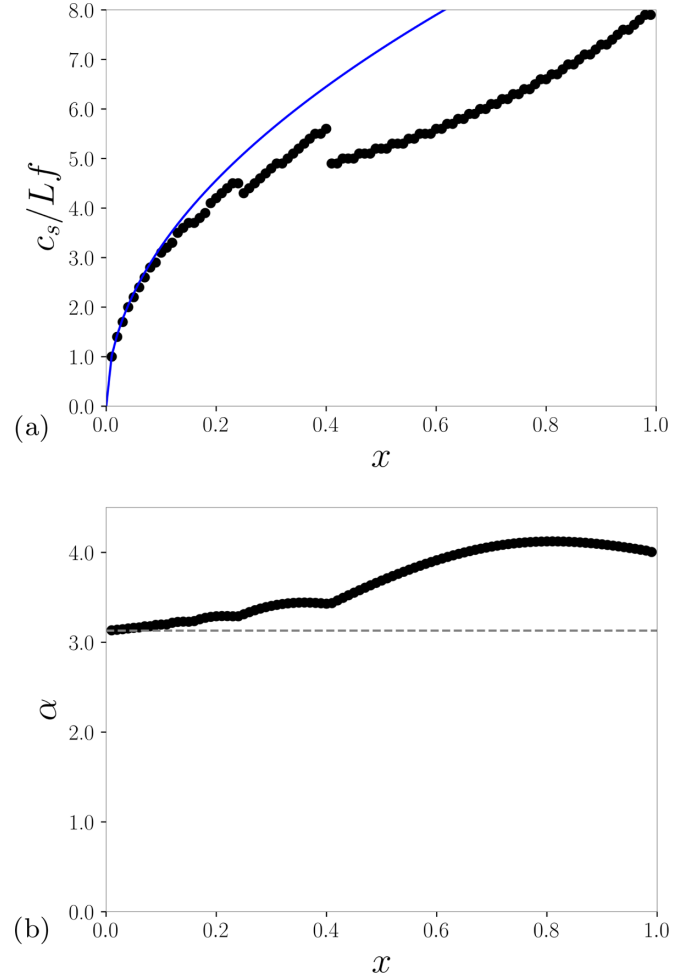


FIG. 4. (a) c_s/Lf as a function of x for the maximal α value found in simulation along a vertical line in Fig. 3(b). The blue solid curve corresponds to the model $c_s/Lf = 10.2\sqrt{x}$. (b) Maximal α value as a function of x . The horizontal dotted line emphasizes the value 3.13 obtained with a simple spring-mass model (Appendix A).

main trend and avoid any additional complexity associated to our specific system.

Our study shows that the energy transfer factor can be up to four times larger in comparison to an actuator without a soft layer, if the parameters are well tuned. This factor is notably higher than the 3.1 factor obtained with bilayered projectiles [27]. For applications, it is relevant to express the values using the mass of the projectile $m = \rho_r S L_r$. This gives $c_s/L_s f = 8.4$ and $m/\rho_s S L_s = 0.32$ for the optimal case.

IV. ANALYTICAL APPROACH

In this section, we show analytically that the complex landscape of the transfer energy factor is directly associated to the propagation properties inside the soft elastic layer. The projectile is considered fully rigid and is modeled by a point mass located in $y = L_s$.

From $t = 0$, the actuator initiates its motion with the velocity $V_p(t) = A\omega \sin(\omega t)$ with $\omega = 2\pi f$. This triggers the propagation of waves inside the soft layer. In fact, the local velocity $v(y, t)$ and deformation $\epsilon(y, t)$ inside the elastic layer

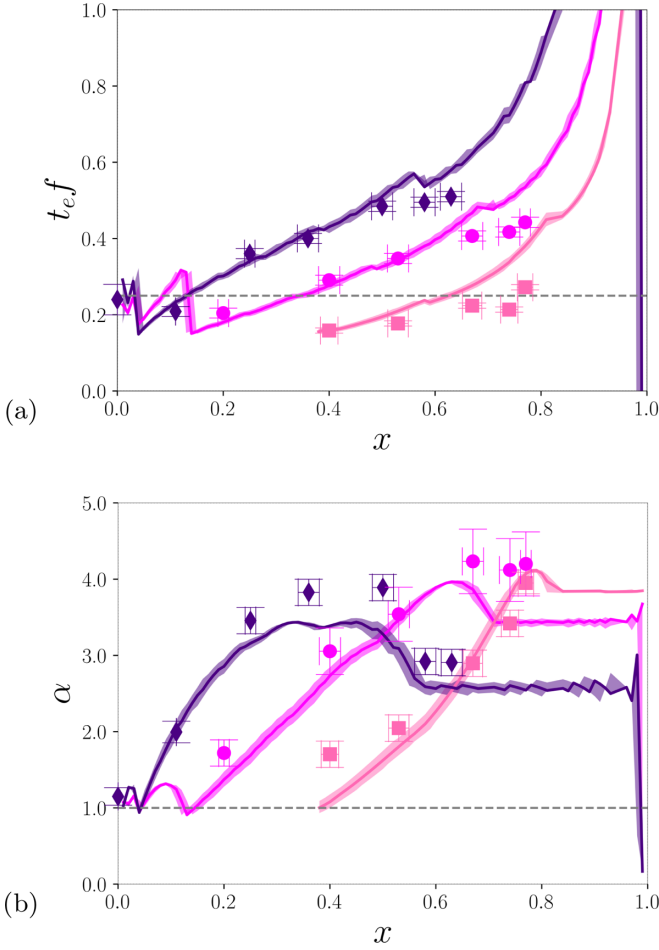


FIG. 5. Comparison between experiments and simulations along the three lines displayed in Fig. 3 (same symbols). $t_e f$ (a) and α (b) are represented as functions of x . Horizontal dashed lines indicate the predictions of an actuator without a soft layer. The thickness of the lines obtained in simulation represents the experimental uncertainty of the quantity $c_s/L_r f$.

are coupled through the equations

$$\begin{aligned} \frac{\partial \epsilon}{\partial t} &= \frac{\partial v}{\partial y}, \\ \frac{\partial v}{\partial t} &= c_s^2 \frac{\partial \epsilon}{\partial y}. \end{aligned} \quad (4)$$

The wave is composed of two components, one propagating in the direction of increasing y and one propagating in the direction of decreasing y . We note $v_+(y, t) = v_+(\xi = t - y/c)$ and $v_-(y, t) = v_-(\zeta = t + y/c)$ respectively as the components of the velocity $v = v_+ + v_-$, while $\epsilon_+(y, t) = \epsilon_+(\xi = t - y/c)$ and $\epsilon_-(y, t) = \epsilon_-(\zeta = t + y/c)$ stand for the deformation $\epsilon = \epsilon_+ + \epsilon_-$. From Eqs. (4), we have $\frac{dv_+}{d\xi} = -c_s \frac{d\epsilon_+}{d\xi}$ and $\frac{dv_-}{d\zeta} = c_s \frac{d\epsilon_-}{d\zeta}$. This simplifies to $v_+ = -c_s \epsilon_+$ and $v_- = c_s \epsilon_-$ since all these functions are null initially. By continuity in $y = 0$ and $y = L_s$, we have the two boundary conditions:

$$V_p(t) = v_+(0, t) + v_-(0, t), \quad (5)$$

$$V_m(t) = v_+(L_s, t) + v_-(L_s, t), \quad (6)$$

where $V_m(t)$ is the velocity of the projectile. First, following these boundary conditions and the propagation properties, we can write

$$v_+(L_s, t) = V_p(t - t_s) - V_m(t - 2t_s) + v_+(L_s, t - 2t_s), \quad (7)$$

with $t_s = L_s/c_s$ being the time to propagate through the soft layer. The expression emphasizes that the state of $v_+(L_s, t)$ at time t depends on the dynamics of the actuator and of the rigid part at earlier instants ($t - t_s$ and $t - 2t_s$, respectively) as well as on $v_+(L_s, t - 2t_s)$. Following this recursive process we can express $v_+(L_s, t)$ as a function of V_p and V_m only:

$$\begin{aligned} v_+(L_s, t) &= V_p(t - t_s) - V_m(t - 2t_s) + V_p(t - 3t_s) - V_m(t - 4t_s) \\ &\quad + V_p(t - 5t_s) - V_m(t - 6t_s) + \dots \end{aligned} \quad (8)$$

Second, the dynamics of the rigid layer is obtained with a simple momentum balance:

$$m \frac{dV_m}{dt}(t) = -E_s S \epsilon(L_s, t) = \frac{E_s S}{c_s} [v_+(L_s, t) - v_-(L_s, t)]$$

or

$$\tau \frac{dV_m}{dt}(t) + V_m(t) = 2v_+(L_s, t), \quad (9)$$

with $\tau = \frac{m c_s}{E_s S} = (1 - x) \frac{\rho_r L}{\rho_s c_s}$ [note that $f\tau = (1 - x) \frac{\rho_r L f}{\rho_s c_s}$]. $v_+(L_s, t)$ is thus the relevant term that sets the dynamics of the rigid layer. This term is itself coupled to the past history of the catapult and rigid layer motions through Eq. (8). In what follows, we distinguish several time intervals.

Note that, in the first time interval, from $t = 0$ to t_s , $v_+(L_s, t) = 0$, since the wave does not have time to travel from $z = 0$ to L_s . As a consequence there is no force applied on the rigid layer, $V_m(t) = 0$, and the projectile does not take off whatever the parameters.

A. Second time interval, from $t = t_s$ to $3t_s$

Only the first term is non-null on the right-hand side of Eq. (8) and $v_+(L_s, t) = V_p(t - t_s)$. As a consequence, the dynamics of the rigid layer is given by

$$\tau \frac{dV_m}{dt} + V_m = 2A\omega \sin[\omega(t - t_s)]. \quad (10)$$

With the condition $V_m(t = t_s) = 0$, it leads to

$$\begin{aligned} V_m(t) &= \frac{2A\omega}{1 + (\omega\tau)^2} [(\omega\tau) \{e^{-(t-t_s)/\tau} - \cos[\omega(t - t_s)]\} \\ &\quad + \sin[\omega(t - t_s)]]. \end{aligned} \quad (11)$$

The ejection condition is written $dV_m/dt(t_e) = 0$, which leads to an implicit equation for t_e

$$e^{-(t_e-t_s)/\tau} = (\omega\tau) \sin[\omega(t_e - t_s)] + \cos[\omega(t_e - t_s)], \quad (12)$$

or we can write a relation between $\alpha = (V_e/A\omega)^2$, with $V_e = V_m(t_e)$, and $\omega(t_e - t_s)$ from Eq. (10):

$$\alpha = 4 \sin[\omega(t_e - t_s)]^2. \quad (13)$$

In Fig. 6, we plot $t_e f$ and α as functions of x and $c_s/L_r f$ as we did in Fig. 3 for the numerical approach. Both approaches match very well for t_e in the range $t_s - 3t_s$ and we can now

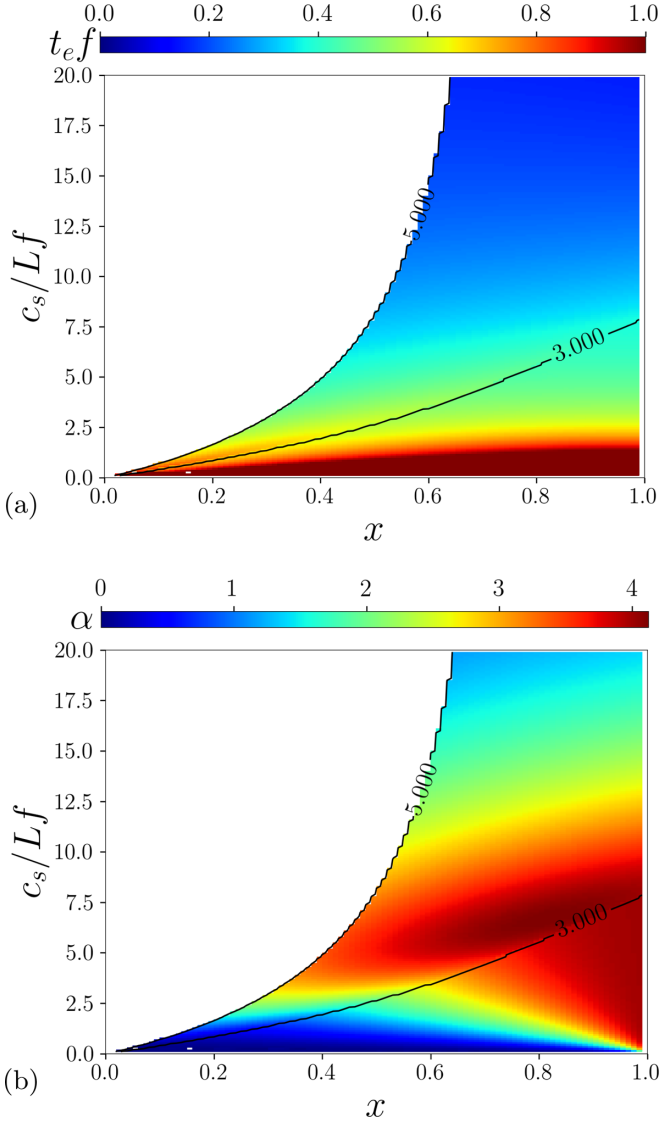


FIG. 6. $t_e f$ (a) and α (b) as functions of c_s/Lf and x calculated by the analytical approach in the time intervals $t_s \leq t_e \leq 3t_s$ and $3t_s \leq t_e \leq 5t_s$. Black solid lines highlight the values of t_e/t_s that are positive integers and $t_e/t_s = 1$ corresponds to the x axis.

understand some features. From Eq. (13), it is obvious that the maximum α value is 4 and is obtained for $\omega(t_e - t_s) = \pi/2 [2\pi]$. In Eq. (12), this imposes $\tau = 0$ or $x = 1$ and $\omega(t_e - t_s) = \pi/2$. Since $t_s \leq t_e \leq 3t_s$, a solution $\alpha = 4$ exists in this time interval for $0 \leq c_s/Lf \leq 8$ in good agreement with the numerical simulation. Asymptotics are calculated in Appendix C for the two limits $x = 1$ and $c_s/Lf = 0$.

B. Third time interval, from $t = 3t_s$ to $5t_s$

If the projectile does not take off in the second interval, we need to consider the next time interval. For $t = 3t_s$ to $5t_s$, $v_+(L_s, t) = V_p(t - t_s) - V_m(t - 2t_s) + V_p(t - 3t_s)$ in Eq. (8). At the onset of this time interval, we have the initial condition $V_m(t = 3t_s) = 2A\omega \frac{(\omega\tau)e^{-2\omega\tau} - (\omega\tau)\cos(2\omega t_s) + \sin(2\omega t_s)}{1 + (\omega\tau)^2}$.

The evolution of the projectile is given by

$$\begin{aligned} \tau \frac{dV_m}{dt} + V_m &= 2A\omega[\sin[\omega(t - t_s)] + \sin[\omega(t - 3t_s)]] \\ &\quad - \frac{2}{1 + (\omega\tau)^2}((\omega\tau)e^{-(t-3t_s)/\tau} \\ &\quad - (\omega\tau)\cos[\omega(t - 3t_s)] \\ &\quad + \sin[\omega(t - 3t_s)]). \end{aligned} \quad (14)$$

Again $t_e f$ and α are obtained in this time interval with the condition $dV_m/dt(t_e) = 0$, which can be solved either numerically or semianalytically. As observed in Figs. 3 and 6, there is a very good agreement and the maximum $\alpha = 4.12$ for $x = 0.8$ and $c_s/Lf = 6.7$ is recovered in this interval. A small difference can however be observed in the region where $c_s/Lf < 2.0$ and $\alpha < 1.0$. This is where successive stages of ejection and reconnection occur in simulation. This behavior is not taken into account in the analytical model.

C. Successive time intervals

The process described above is recursive. We could also obtain results for higher time intervals ($t > 5t_s$) but the analytical expressions become very long. Nevertheless, we observe in Fig. 6 that the odd values of t_e/t_s separate domains that seemed discontinuous (or at least the partial derivatives seem discontinuous) in Fig. 3. This is particularly striking in the α diagram and for $t_e/t_s = 3$. In light of our calculations, this corresponds to a change in the expressions of the takeoff time and velocity and is directly linked to the number of travels of the wave propagating back and forth inside the soft elastic layer. It shows that the maximum of efficiency, $\alpha = 4.12$, is found as the rigid layer takes off between $3t_s$ and $5t_s$. For $t_s < t_e < 3t_s$ a local maximum of $\alpha = 4$ is found as $x = 1$. For $t_e > 5t_s$ the efficiency decreases and we rely on the numerical simulations to obtain the values.

V. CONCLUSION

In this study we have shown that adding a soft layer at the distal end of an actuator can increase the ejection efficiency by more than a factor 4. This result is supported by experimental, numerical, and analytical approaches. High efficiency requires the compliant layer to have a thickness and a rigidity that match both the mass of the projectile and the frequency of the actuator. More precisely, the efficiency is maximal, with a value around 4.12, for $x = 0.8$ and $c_s/Lf = 6.7$, or $c_s/Ls f = 8.4$ and $m/\rho_s L_s = 0.32$, if expressed with the mass of the projectile.

Importantly we emphasize that a thick soft layer, $x \simeq 1$, gives an efficiency equal to 4 for a large range of rigidity since in that case $c_s/Lf \leq 8$ only is required. This case is almost as good as the optimal case but has the advantage of being more adaptable. A very thick and soft layer could potentially be used with numerous projectiles and actuators. This study shows that both efficiency and flexibility could be obtained simultaneously with a smart choice of the compliant layer for applications requiring actuation of an object.

ACKNOWLEDGMENTS

G.G. acknowledges financial support by the French Ministry of Armed Forces, Agence de l'Innovation Defense (Defence Innovation Agency).

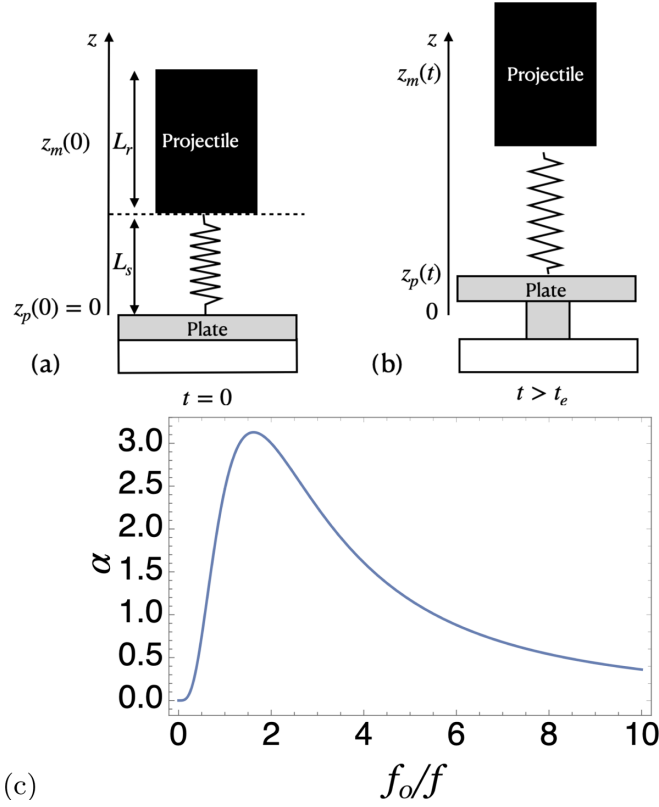


FIG. 7. (a),(b) Description of the spring-mass system. (c) Energy transfer factor α as a function of the frequency ratio f_0/f .

APPENDIX A: SPRING-MASS SYSTEM

The spring-mass system is described in Celestini *et al.* [27]: the projectile of mass m is rigid and the soft layer consists in a massless linear spring with a stiffness k as sketched in Fig. 7(a). The initial distance between the center of mass of the projectile and the plate of the actuator is still $L_s + L_r/2$ and the position of the plate undergoes a harmonic variation given by $z_p(t) = A[1 - \cos(2\pi ft)]$, with a frequency f and an amplitude A . The maximum velocity of the plate is $V_p^* = 2\pi fA$.

Between 0 and t_e , respectively the initial and ejection times, the position $z_m(t)$ of the projectile is given by the equation

$$\ddot{z}_m(t) = -(2\pi f_0)^2 [z_m(t) - z_p(t) - (L_s + L_r/2)], \quad (\text{A1})$$

where the acceleration of the projectile \ddot{z}_m is balanced by the spring force, which is proportional to the elongation $z_m - z_p - (L_s + L_r/2)$. We denote by $f_0 = \frac{1}{2\pi} \sqrt{\frac{k}{m}}$ the eigenfrequency of the spring-mass system. The solution of this forced harmonic oscillator equation, with $z_m(0) = L_s + L_r/2$ and $\dot{z}_m(0) = 0$, is written

$$z_m(t) = L_s + L_r/2 + A + \frac{A}{f^2 - f_0^2} \times [f_0^2 \cos(2\pi ft) - f^2 \cos(2\pi f_0 t)]. \quad (\text{A2})$$

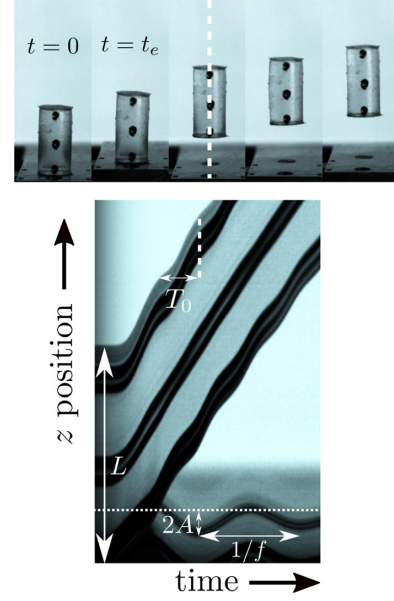


FIG. 8. (Top) Typical image sequence of a soft layer ejection. (Bottom) Space-time diagram built along the vertical line passing through the center of the soft layer.

The projectile takes off when the elastic response of the spring equals zero, because the projectile is not attached to the soft layer. Hence the condition $z_m - z_p = L_s + L_r/2$ in Eq. (A2) gives the ejection time t_e :

$$t_e = \frac{1}{f + f_0}. \quad (\text{A3})$$

We note the velocity of the projectile at ejection $V_e = \dot{z}_m(t_e)$. The velocity ratio at takeoff, V_e/V_p^* , is found to be

$$V_e/V_p^* = \frac{\dot{z}_m(t_e)}{2\pi fA} = \frac{f_0/f}{f_0/f - 1} \sin\left(\frac{2\pi}{f_0/f + 1}\right). \quad (\text{A4})$$

We define the energy transfer factor as $\alpha = (V_e/V_p^*)^2$: it measures the ratio of the kinetic energy of the projectile ejected to those of the kinetic energy of the projectile moving at the maximum velocity of the plate. For $f_0/f \simeq 1.62$, the energy transfer factor $\alpha = (V_e/V_p^*)^2$ is maximal and equals 3.13.

APPENDIX B: MEASUREMENT OF THE WAVE VELOCITY IN THE SOFT LAYER

The wave velocity inside the soft layer is obtained by measuring the eigenperiod T_0 of the free oscillations of soft layers of several lengths L_s . Free soft layers were ejected alone with the throwing engine. A typical image sequence is displayed in Fig. 8 together with a space-time diagram built along the vertical line passing through the center of the soft layer. Once ejected, the first eigenmode is clearly observed and the period is measured for each layer. T_0 is plotted as a function of L_s in Fig. 9. We observe that both quantities are proportional with a constant $a = (0.256 \pm 0.008) \text{ s}^{-1}$. We deduce $c_s = 2L_s/T_0 = 2/a = (7.8 \pm 0.3) \text{ m s}^{-1}$.

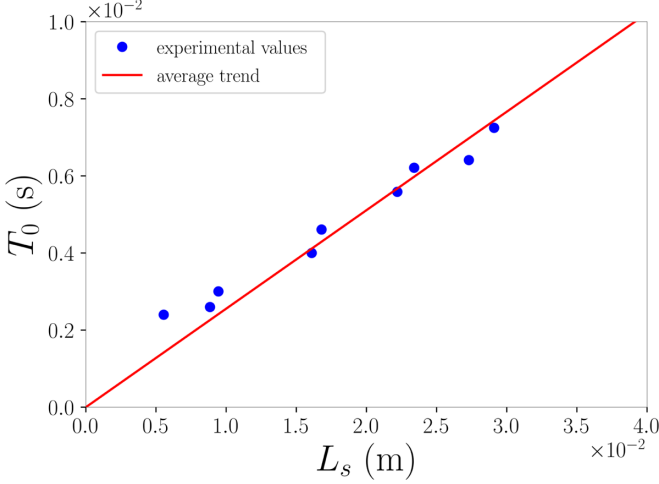


FIG. 9. Measurements of the eigenperiod T_0 of the soft layer as a function of its length L_s . The solid line is the best proportional relation with a constant equal to 0.256 s m^{-1} .

APPENDIX C: SOME COMPUTATIONS IN THE INTERVAL

$$t_s \leq t \leq 3t_s$$

Here, we would like to get some asymptotic of Eq. (12):

$$e^{-(t_e - t_s)/\tau} = (\omega\tau) \sin[\omega(t_e - t_s)] + \cos[\omega(t_e - t_s)]. \quad (\text{C1})$$

By introducing the new variable \tilde{t} , with $t_e = t_s + \tilde{t}/\omega$, we obtain the implicit equation

$$e^{-\frac{\tilde{t}}{\omega\tau}} = \omega\tau \sin \tilde{t} + \cos \tilde{t}. \quad (\text{C2})$$

(i) As $\omega\tau$ tends to zero, the exponential tends to zero and the implicit equation is solved as the cosine tends also to zero; this yields

$$\tilde{t} \rightarrow \frac{\pi}{2} + \omega\tau + e^{-\frac{\pi}{2\omega\tau}},$$

which remains valid until $\omega\tau \sim 1$. It predicts

$$\alpha \sim 4 - 2(\omega\tau + e^{-\frac{\pi}{2\omega\tau}})^2,$$

as $x \rightarrow 1$.

(ii) In the opposite limit, i.e., $\omega\tau \rightarrow \infty$,

$$\tilde{t} \rightarrow \pi - \frac{2}{\omega\tau} + \frac{\pi}{(\omega\tau)^2},$$

such that

$$\alpha \sim \frac{16}{(\omega\tau)^2},$$

as $\omega\tau \rightarrow \infty$, i.e., $c_s/Lf \rightarrow 0$.

APPENDIX D: DESCRIPTION OF THE PLATE MOTION BY THE EQUATION OF THE DAMPED HARMONIC OSCILLATOR

1. Equations

We consider here that the engine plate follows the motion of a damped harmonic oscillator given by

$$\ddot{z}_p(t) + 2\zeta\omega\dot{z}_p(t) + \omega^2 z_p(t) = \omega^2 A, \quad (\text{D1})$$

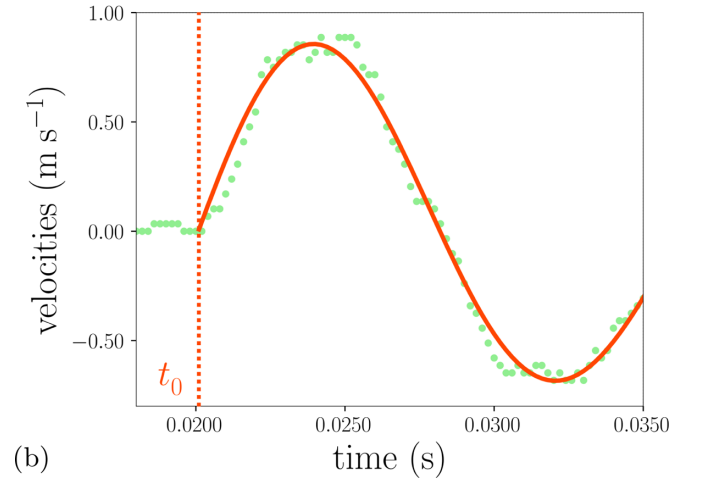
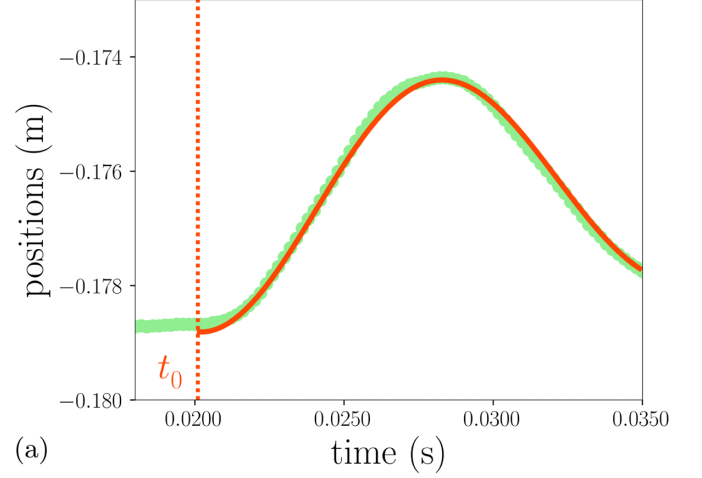


FIG. 10. Typical interpolation of the plate motion. The parameters of the interpolation are $t_0 = 0.0204 \text{ s}$, $f = 63.2 \text{ Hz}$, and $\zeta = 6.4 \times 10^{-2}$.

with ζ the damping ratio and $\omega = 2\pi f$ the angular frequency. After integration with the two initial conditions $z_p(0) = 0$ and $\dot{z}_p(0) = 0$, the plate motion is written

$$z_p(t) = A \left[1 - e^{-\zeta\omega t} \left(\cos(\omega_d t) + \frac{\zeta\omega}{\omega_d} \sin(\omega_d t) \right) \right], \quad (\text{D2})$$

with $\omega_d = \omega\sqrt{1 - \zeta^2}$ the pseudofrequency of the engine plate. The time evolution of the plate velocity and acceleration are given by

$$\begin{aligned} \dot{z}_p(t) &= A e^{-\zeta\omega t} \left(\omega_d + \frac{\zeta^2\omega^2}{\omega_d} \right) \sin(\omega_d t), \\ \ddot{z}_p(t) &= A e^{-\zeta\omega t} \left(\omega_d + \frac{\zeta^2\omega^2}{\omega_d} \right) [\omega_d \cos(\omega_d t) - \zeta\omega \sin(\omega_d t)]. \end{aligned} \quad (\text{D3})$$

The plate maximal velocity is reached at time t_v that verifies $\ddot{z}(t_v) = 0$; hence $t_v = \frac{1}{\omega\sqrt{1 - \zeta^2}} \arctan\left(\frac{\sqrt{1 - \zeta^2}}{\zeta}\right)$. The maximum velocity of the engine plate, V_p^* , is slightly lower than $A\omega$,

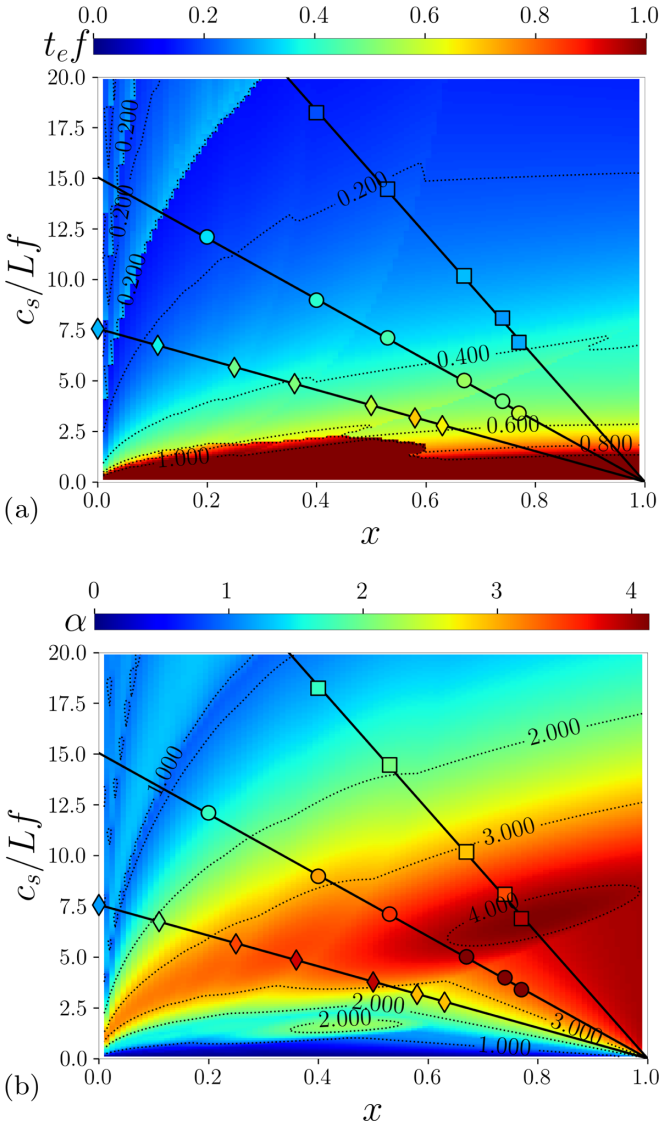


FIG. 11. Comparison between experiments and simulations in the case of an underdamped oscillator: $t_e f$ (a) and α (b) as functions of x and c_s/Lf . The three sets of experiments correspond to $c_s/Lf = 7.57$ (diamonds), 15.1 (disks), and 34.5 (squares).

the expression obtained with a harmonic plate motion, and written

$$V_p^* = \dot{z}(t = t_v) = A\omega e^{-\frac{\zeta}{\sqrt{1-\zeta^2}} \arctan\left(\frac{\sqrt{1-\zeta^2}}{\zeta}\right)}. \quad (\text{D4})$$

2. Experimental measurements

The parameters f (or $\omega = 2\pi f$) and ζ are directly obtained by interpolating the position of the engine plate as a function of time (Fig. 10). It is found experimentally that ζ is constant whatever the experiment and equals $(6.4 \pm 0.3) \times 10^{-2}$. The ejection engine was tuned with two configurations, one with $f = 31.2 \pm 0.1$ Hz and the other one with 63.2 ± 0.1 Hz. Note that the interpolation is also used to define precisely the initiation time of the plate motion, noted t_0 . In the main text and in Fig. 2, we have defined the time axis with respect to t_0

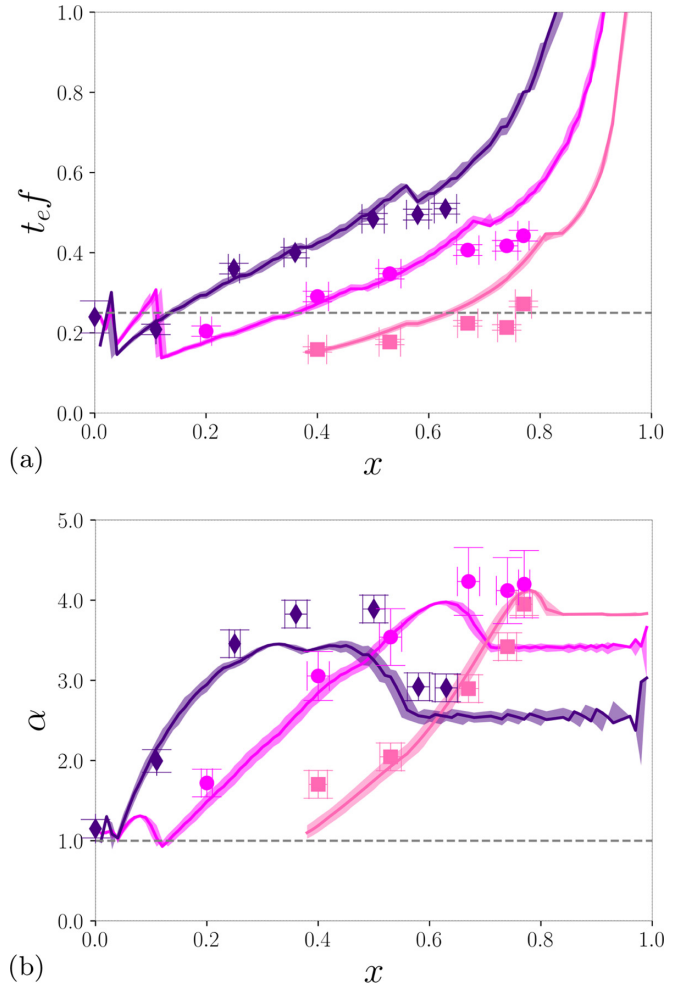


FIG. 12. Comparison between experiments and simulations (underdamped case) along the three lines displayed in Fig. 11 (same symbols). $t_e f$ (a) and α (b) are represented as functions of x . Horizontal dashed lines indicate the predictions of an actuator without the soft layer.

so that $t = 0$ corresponds to the initiation of the plate motion as expected from the interpolation.

3. Underdamped harmonic motion in simulation

Simulations have been performed assuming that the engine plate performs the motion of an underdamped harmonic oscillator. Like in experiments, the energy transfer factor is defined with both the ejection velocity and the maximal velocity of the plate, but the latter is now given by Eq. (D4). Results are displayed in Figs. 11 and 12 and can be compared to the case of the ideal harmonic oscillator (Figs. 3 and 5). The two cases give similar results. The differences around the experimental data points Figs. 12(a) and 12(b) do not exceed a few percent and are not significant enough to claim that the damping plays a major role in the dynamics of the system.

APPENDIX E: PHYSICAL QUANTITIES AND VALUES

For more clarity, symbols used in the text are referenced in Table I.

TABLE I. Summary of the symbols used in the text, associated with the physical quantities they represent and their typical values if existing.

Symbol	Quantity	Value
α	Energy transfer factor	
ϵ	Local deformation in the soft layer	
ϵ_+	Deformation towards the increasing z	
ϵ_-	Deformation towards the decreasing z	
ζ	Damping ratio	0.064
ρ_r	Density of the projectile	1300 kg m ⁻³
ρ_s	Density of the soft layer	1000 kg m ⁻³
ω	Angular frequency of the plate	
ω_d	Pseudofrequency of the plate	
A	Plate loading amplitude	~2 mm
E_r	Young's modulus of the projectile	3.6 GPa
E_s	Young's modulus of the soft layer	~61 kPa
L	Total length of the soft layer-projectile system	10.2–45.4 mm
L_r	Projectile length	8.2–16.3 mm
L_s	Soft layer length	2.0–29.1 mm
S	Cross section of the projectile-soft layer	
T_0	Eigenperiod of the soft layer in free flight	~10 ms
V_e	Ejection velocity of the projectile	~1 m s ⁻¹
V_p	Plate velocity	
V_p^*	Maximal velocity of the plate	~1 m s ⁻¹
V_m	Projectile velocity	
c_r	Wave velocity in the projectile	1700 m s ⁻¹
c_s	Wave velocity in the soft layer	7.8 m s ⁻¹
f_0	Eigenfrequency of the spring-mass system	
f	Plate frequency	31.1–63.2 Hz
k	Spring stiffness	
m	Mass of the projectile	
t_0	Initiation time of the plate motion	
t_e	Ejection time	
t_s	Travel time of the wave through the soft layer	0.26–3.73 ms
t_v	Time of maximal velocity of the damped oscillator	
u	Displacement field	
u_r	Displacement in the projectile	
u_s	Displacement in the soft layer	
v	Local velocity in the soft layer	
v_+	Component of v propagating towards increasing z	
v_-	Component of v propagating towards decreasing z	
x	Ratio between the length of the soft layer and the total length	0–1
y	Longitudinal coordinate within the projectile-soft layer frame	
y_c	Contact point between the projectile and the soft layer	
z	Longitudinal coordinate in the laboratory frame	
z_m	Projectile position	
z_p	Plate position	

[1] R. M. Alexander and H. C. Bennet-Clark, Storage of elastic strain energy in muscle and other tissues, *Nature (London)* **265**, 114 (1977).

[2] A. L. Hof, B. A. Geelen, and J. Van den Berg, Calf muscle moment, work and efficiency in level walking; Role of series elasticity, *J. Biomech.* **16**, 523 (1983).

[3] G. J. Ettema, Mechanical efficiency and efficiency of storage and release of series elastic energy in skeletal muscle during stretch-shorten cycles., *J. Exp. Biol.* **199**, 1983 (1996).

[4] T. J. Roberts, The integrated function of muscles and tendons during locomotion, *Comp. Biochem. Physiol. Part A: Mol. Integr. Physiol.* **133**, 1087 (2002).

[5] T. J. Roberts and E. Azizi, Flexible mechanisms: The diverse roles of biological springs in vertebrate movement, *J. Exp. Biol.* **214**, 353 (2011).

[6] R. L. Marsh and H. B. John-Alder, Jumping performance of hylid frogs measured with high-speed cine film, *J. Exp. Biol.* **188**, 131 (1994).

- [7] K. Kubo, Y. Kawakami, and T. Fukunaga, Influence of elastic properties of tendon structures on jump performance in humans, *J. Appl. Physiol.* **87**, 2090 (1999).
- [8] M. Burrows, Froghopper insects leap to new heights, *Nature (London)* **424**, 509 (2003).
- [9] H. C. Astley and T. J. Roberts, Evidence for a vertebrate catapult: Elastic energy storage in the plantaris tendon during frog jumping, *Biol. Lett.* **8**, 386 (2012).
- [10] T. J. Roberts, R. L. Marsh, P. G. Weyand, and C. R. Taylor, Muscular force in running turkeys: The economy of minimizing work, *Science* **275**, 1113 (1997).
- [11] A. M. Wilson, J. C. Watson, and G. A. Lichtwark, A catapult action for rapid limb protraction, *Nature (London)* **421**, 35 (2003).
- [12] N. T. Roach, M. Venkadesan, M. J. Rainbow, and D. E. Lieberman, Elastic energy storage in the shoulder and the evolution of high-speed throwing in homo, *Nature (London)* **498**, 483 (2013).
- [13] N. T. Roach and D. E. Lieberman, Upper body contributions to power generation during rapid, overhand throwing in humans, *J. Exp. Biol.* **217**, 2139 (2014).
- [14] T. J. Roberts and R. L. Marsh, Probing the limits to muscle-powered accelerations: Lessons from jumping bullfrogs, *J. Exp. Biol.* **206**, 2567 (2003).
- [15] D. Paluska and H. Herr, The effect of series elasticity on actuator power and work output: Implications for robotic and prosthetic joint design, *Rob. Auton. Syst.* **54**, 667 (2006).
- [16] J. Aguilar, A. Lesov, K. Wiesenfeld, and D. I. Goldman, Lift-Off Dynamics in a Simple Jumping Robot, *Phys. Rev. Lett.* **109**, 174301 (2012).
- [17] M. Grebenstein, M. Chalon, W. Friedl, S. Haddadin, T. Wimböck, G. Hirzinger, and R. Siegwart, The hand of the DLR hand arm system: Designed for interaction, *Int. J. Rob. Res.* **31**, 1531 (2012).
- [18] D. Braun, M. Howard, and S. Vijayakumar, Optimal variable stiffness control: Formulation and application to explosive movement tasks, *Auton. Robot.* **33**, 237 (2012).
- [19] D. W. Haldane, M. M. Plecnik, J. K. Yim, and R. S. Fearing, Robotic vertical jumping agility via series-elastic power modulation, *Sci. Rob.* **1**, eaag2048 (2016).
- [20] M. Ilton, M. S. Bhamla, X. Ma, S. M. Cox, L. L. Fitchett, Y. Kim, J.-s. Koh, D. Krishnamurthy, C.-Y. Kuo, F. Z. Temel, A. J. Crosby, M. Prakash, G. P. Sutton, R. J. Wood, E. Azizi, S. Bergbreiter, and S. N. Patek, The principles of cascading power limits in small, fast biological and engineered systems, *Science* **360**, eaao1082 (2018).
- [21] C. Cohen and C. Clanet, Physics of ball sports, *Europhys. News* **47**, 13 (2016).
- [22] M. Phomsoupha, G. Laffaye, C. Cohen, and C. Clanet, How to use the elasticity of a badminton racket to increase its speed by 80%?, *Comput. Methods Biomech. Biomed. Eng.* **18**, 2028 (2015).
- [23] J. S. B. Mather, M. J. Smith, S. Jowett, K. a. H. Gibson, and D. Moynihan, Application of a photogrammetric technique to golf club evaluation, *Sports Eng.* **3**, 37 (2000).
- [24] J. Worobets and D. Stefanyshyn, The influence of golf club shaft stiffness on clubhead kinematics at ball impact, *Sports Biomech.* **11**, 239 (2012).
- [25] S. J. MacKenzie and D. E. Boucher, The influence of golf shaft stiffness on grip and clubhead kinematics, *J. Sports Sci.* **35**, 105 (2017).
- [26] C. Raufaste, G. R. Chagas, T. Darmanin, C. Claudet, F. Guittard, and F. Celestini, Superpropulsion of Droplets and Soft Elastic Solids, *Phys. Rev. Lett.* **119**, 108001 (2017).
- [27] F. Celestini, J. Mathiesen, M. Argentina, and C. Raufaste, Contact Layer as a Propelling Advantage in Throwing, *Phys. Rev. Appl.* **14**, 044026 (2020).
- [28] See Supplemental Material at <http://link.aps.org/supplemental/10.1103/PhysRevE.105.025001> for videos of the experiments.
- [29] M. Czerner, L. S. Fellay, M. P. Suárez, P. M. Frontini, and L. A. Fasce, Determination of elastic modulus of gelatin gels by indentation experiments, *Proc. Mater. Sci.* **8**, 287 (2015).